Detection of sea ice floe flooding in the Southern Ocean using Sentinel-1 SAR imagery.

Jullian C.B. Williams[1,2], Stephen F. Ackley[2], Alberto M. Mestas-Nuñez[2], Grant J. Macdonald[2,3], Stefanie Arndt[4]

[1] Department of Mathematics and Information Technology, The University of the Commonwealth Caribbean, Kingston, Jamaica.
[2] NASA Center for Advanced Measurements in Extreme Environments (CAMEE), University of Texas at San Antonio, San Antonio, TX 78249, USA.
[3] University of Victoria, Department of Geography, Victoria, BC, CA.
[4] Alfred-Wegener-Institut, Helmholtz-Zentrum für Polar- und Meeresforschung, Bremerhaven, Germany
Correspondence to: Julllian C.B. Williams (williamsjcbw@gmail.com)

Abstract

During the summer months in the Antarctic, perennial and seasonal sea ice floes flood. Flooding is caused by snow at the surface weighing down the ice, causing a negative freeboard and flooding the basal snow layer with seawater. This creates a brine-slush layer. Alternatively, or simultaneously, meltwater can percolate through the snow and flood the surface of the ice floe. The appearance of these flooded ice floes changes dramatically in synthetic aperture radar (SAR) scenes with season and as the dielectric constant changes with brine content. In addition to this, the incident look angle of the radar imager affects the returned backscatter intensity across the scene.

The Sentinel-1 instrument began collecting data with its S1A instrument in 2014 and later S1B in 2016 and continues to acquire SAR data across the globe. Sentinel-1 supplies an unprecedented, dual-band look at sea ice in the North and

South poles to understand the dynamics of sea ice processes during polar nighttime. The satellite instrument provides a unique opportunity to study the signal attenuations and the subsequent backscatter intensities in the SAR scene that change with seasonal ice flooding. This paper uses the Sentinel-1 radar data to understand the changes in backscatter intensity in flooded floes in the Amundsen, whose changes in floe flooding show spatial and spectral changes throughout the seasons.

Introduction

In the Southern Ocean, snow-ice is a mappable ice unit. Snow ice forms across the Antarctic pack ice zone and is one of the primary contributors to the sea-ice mass balance (Ackley et al., 2020; Tian et al., 2020; Jeffries et al., 2001; Worby et al.,1998; Eicken et al.,1994). Therefore, understanding the process of its formation is integral to Antarctic Sea ice cycles, especially in the Amundsen and Weddell Sea. The process of snow-ice formation is a cycle that can help maintain the equilibrium between the bottom melting of the ice floe and freezing of the flooded snowpack in contact with the depressed ice floe (Lytle and Ackley, 2001). There are two distinct functions in snow-ice formation. Figure 1 illustrates the depression of the ice floe below sea level, just from the weight of the snow above, resulting in a negative ice freeboard. The initially dry snow is subjected to an influx of sea water, creating a slushy basal layer of the snowpack above the floe (Ackley et al., 2020).

Figure 1: Initial ice floe (a) and its subsequent depression (b) resulting in negative freeboard and slush layer from weighted snowpack. The total snow ice height in (c) includes the dry snow and slush layer while the bottom melt begins from warm water below. Snow ice is formed in (d) and as the bottom melt advances, the freeboard includes the snow-ice formation. The total ice thickness remains unchanged in this example since the rate of bottom ice melting is equivalent to the new snow ice formed above. Annotations: F: freeboard height (-F: negative freeboard height), S: snow height, Sdry: dry snow height, Swet: wet snow height, ST: total snow height, I: Ice height.

While this process occurs above the ice surface, the recession of ice from bottom melting can also occur. Warm water melts the base of the ice, gradually receding the initial ice type. The newly formed snow-ice will eventually consolidate above the initial ice floe with decreasing temperature. As the ice melts below the ice pack with increasing water temperature in the summer as shown in Figure 2 (left-hand side), snow-ice is formed from the slush layer when the ice temperature is lowered in the winter (right-hand side).

Figure 2: "Vertical conveyor belt" behavior of snow-ice formation from snow depression and bottom-ice melt (left) and consolidation of slush layer above initial ice formation adapted from Ackley, et al. 2020.

This is a vertical, cyclical process of ice destruction and formation that is described as a "vertical conveyor belt" of ice formation that dominates the Western-Amundsen ice field (Ackley et al., 2020). It is unsurprising that this new, snow-ice formation displays distinguishing physical characteristics in both in-situ and remote sensing techniques.

Distinguishing snow-ice from the initial in-situ pack ice requires a multi-criteria approach from field measurements. Ackley et al. (2020) describe a bulk parameterization and residual method to derive the variation and magnitude of the ocean heat flux. This analysis is supported by a time series temperature record from the snowpack to capture the advancement of the flooded layer's depth. The progression of ice floe flooding can also occur from periodic increases in the local snowpack either from accumulation or redistribution of snow (snow drifting under high winds) (Perovich et al., 2004; Lytle and Ackley, 2001; Massom et al., 2001; Maksym and Jeffries, 2001; Jeffries et al.,1994) and this is particularly noticeable in the Weddell Sea. However, in the case of the Amundsen, ice floe flooding has been discussed by Ackley et al. (2020) as a function of summer ice bottom melting reducing the thickness of the ice profile (Figure 2). The weight of the snowpack above the receding ice column bears down below sea level, flooding the base level of the snowpack. This slushy layer of ice is eventually frozen to form snow-ice. In winter conditions, Lytle and Ackley (2001) describe a series of in-situ measurements taken to confirm snow-ice layers in the ice pack. Air temperature, wind speed, and water temperature (just below the sea ice) readings were taken at or within 200 m from a lead in the Weddell Sea. In addition to this, ice cores were taken to derive the bulk salinity, isotope ratio, and thickness. However, in the Amundsen snow-ice formation is bound to specific segments of the region. Ackley et al. (2020) describe the snow-ice concentrated regions being to the Eastern segment of the Amundsen Sea. This is supported by buoy-derived ice thickness profiles derived from the densities of sea water, snow, slush and ice. The thickness-by-day plots display a reduced change in the total ice thickness derived by deployed buoys and upward-looking sonar. This reduction is evidence of the “conveyor-belt” behavior of the ice since the new snow-ice formation replaces some of the lost bottom ice thickness (Figure 2).

Supporting the mechanism of snow-ice formation is a geochemical analysis of the snow-ice column done by Tian et al. (2020). This method analyzed salinity, ice texture, and water isotope ratios to determine the changes in the ice profile. A total of eight (8) ice cores were profiled to determine the variation in salinity and ^{18}O levels with depth and corresponding ice textures. While Tian et al. (2020)

explains that the sample size is not large enough to determine the controls on the evolution of snow-ice, their updated oxygen isotope mixing model provides a lower and upper limit to chemically identify snow-ice formation. Still, the identification of snow-ice versus frazil ice can be difficult to determine due to mixing and diffusion processes during flooding and refreezing of snow-ice (Tian et al., 2020). Nevertheless, the study confirms that the Amundsen Sea is a novel case for snow-ice accumulation.

Snow ice formation is reported on several accounts in the Antarctic (Ackley et al., 2020, Willmes et al., 2011, Arndt et al., 2016, Nicolaus et al., 2009, Lytle and Ackley, 2001) which justifies our motivation to examine this region using remote sensing techniques. The snow-ice may be defined as a texturally anomalous feature in the ice field that brightens and darkens depending on the season and adjacent ice features. The snow-ice in the backscattering field is also affected by icebergs in the field since the higher backscatter intensity of the icebergs skews the surrounding backscatter signatures. Hosseinmostafa et al. (1995) explain that backscatter intensity in SAR imaging systems is notoriously ambiguous, affected by polarization, look angle, dielectric properties, field conditions (melting and freezing periods), and the resultant scattering coefficients. However, flooded and unflooded sections of ice (slush versus no slush layer) show a difference in backscatter intensity as illustrated in Figure 3. The figure suggests that with increasing incidence angle in the co-polarized band (VV), there is separation of flooded and unflooded ice layers with respect to backscatter intensity. However, this appears to be true only up to approximately 55-degrees. The slush layer shows a lower backscatter intensity than the no-slush layer between ~30 to 55-degree angles. This distinction is lost between ~60 to 70-degrees and there afterward highly separable again at ~75-degrees.

Figure 3: Scattering co-efficient (backscatter intensity) versus incidence angle (degrees) with respect to flooded (slush) and unflooded (no-slush) layers in first year ice adapted from Hosseinmostafa et al. (1995).

Sentinel-1 has an incidence angle range from ~16-46 degrees and a Maximum Noise Equivalent Sigma Zero of ~ -22-dB. Still, nominal backscatter intensities can reach and exceed the -30-dB mark. Therefore, the separation of flooded (slush) and unflooded (ice) is possible, especially when texture analysis is included (Lohse et al., 2021; Murashkin et al., 2019; Scharien et al., 2017; Hosseinmostafa et al., 1995). Investigating the probability density functions (PDFs) in multiple sections of the Amundsen is also useful to define class regions of snow ice from other features in the ice field. Ozsoy-Cicek et al. (2010) describe using PDFs with radar image data (RADARSAT-1) to define ice types in the Bellingshausen Sea.

The mapping of flooded and potential snow-ice in the Amundsen and Weddell Seas is therefore possible using remote sensing techniques. The Amundsen Sea provides a unique case in which these features regions are concentrated and confirmed by in-situ data. Knowing where their location is concentrated spatially allows us to compare their satellite signatures to other known ice types. This is advantageous since remote sensing techniques can be ambiguous, especially in the case of synthetic aperture radar (SAR) systems. The sensitivity of remote sensing techniques, i.e., atmospheric influences, data availability, band and polarimetric limitations, noise etc., cause uncertainty to distinguish between units in the ice field. However, the concentration of snow-ice in the Amundsen Sea evidenced by field data, gives us ground truth to support our results from satellite-derived information. However, here we also investigate the dynamics of flooded ice from Ackley et al. (2020) and apply them to the Weddell Sea with the ground truth data from the Polarstern cruise to the SW Weddel Sea (PS-124) ice core data.

The changes in the sea ice scene through the seasons can be viewed using satellite imagery. In the summer months, optical imagery can be used to see the ice cover. However, during the winter, optical sensors are inhibited by cloud cover.

Also, since the flooded layer is found below an otherwise intact snow cover, visible imagery cannot be used to detect floodings unless it appears, for example as a melt pond on the surface. Therefore, we view the sea ice scenes using radar images. The doppler system used by radar sensors provides active remote sensing data, free of atmospheric disturbances in the scene. Sentinel-1 provides co- and cross-polarized, cloud-free images from 2016 and is ongoing. Therefore, a time-series approach regarding the development and coverage of surface flooding and snow-ice by season through time can be potentially derived.

The appearance of these flooded ice floes changes dramatically in synthetic aperture radar (SAR) scenes with the seasons and as the dielectric constant changes with brine content. The satellite instrument provides a unique opportunity to study the signal attenuations and the subsequent backscatter intensities in the SAR scene that change with seasonal ice flooding. This study uses Sentinel-1 radar data and remote sensing techniques to understand the changes in backscatter intensity in flooded floes in the Southern seas, whose changes in floe flooding show spatial and spectral changes throughout the seasons.

Study Areas

The study uses the knowledge and framework of flooded sea ice in the North-Eastern flank of the Amundsen Sea (marked in red shown in Figure 4a) to apply remote sensing and geostatistical techniques in the Weddell Sea (Figure 4b).

Macdonald et al. (2023) describe a Sentinel-1 image collection showing the changes in the Amundsen Sea ice field from 2016 to 2021. The timelapse video shows the progression of ice and polynyas in the Amundsen Sea with the centralized Thwaites Glacier as a reference feature. The Amundsen Sea is dotted with icebergs across the images, which were calved from the Thwaites Glacier.

Figure 4a: North-Eastern Amundsen Sea in red box.

Figure 4b: Western Weddell Sea with a drifting buoy track line in green and overlapping satellite and core data from Polarstern 124 region of interest in the red box.

The Western Amundsen is defined by an ice production zone in which an open water polynya produces new ice in the scene. Ice accumulation exists towards the East and North-Eastern segments of the Amundsen. The timelapse illustrates an outflow of newly formed ice from the West to the East of the Amundsen, and from the South to the East and East-North-East of the ice field. This is a consistent, cyclical construction and movement of juvenile ice from the polynya area into the greater Amundsen Sea. Macdonald et al. (2023) describe the bathymetry of the Western Amundsen as a key control on the development and entrainment of newly formed ice. An iceberg “chain” formed by grounded icebergs underlain structural highs, defining newly formed ice from the polynya. Behind the chain, further West is another walled-in structure that forms a secondary polynya. These iceberg walls act as a type of natural groyne for new ice and restrict outflow into the East of the Amundsen and also prevents ice advected into the region from entering the polynya area.

The Eastern Amundsen is starved of new ice produced from its Western flank. The maintenance of ice concentration in the East may therefore not result from young ice congelation influenced by the West, but from snow-ice seated and consolidated above the sea ice within its own system. The Eastern Amundsen has an independent ice production zone from the West. The result is a “Y” shaped confluence about the Twaites Glacier, with icebergs lacing the banks of the severed outflows.

Imaging quantifies some segment of the detection of flooded ice. Still, SAR data is typically ambiguous and validation of this is arduous in synthetic aperture radar data alone. To resolve some of these ambiguities, we use in-situ data and support from IceSat-2 altimetry described in Williams et al., (2022) to verify changes in ice thickness in the flooded ice in the Weddell Sea.

Methods

The total icefield includes the marginal ice zone, where the sea ice front meets the open ocean adjacent to both the Amundsen and Weddell Seas. Therefore, we subset the ice-covered section of the image to enclose the flooded and snow-ice area of the scene. First, we use the Amundsen as a form of "ground-truth" and investigate the mean backscatter intensity of the flooded ice in March 2018. Next, the subset image is used to train the flooded ice objects and snow-ice cover. Google Earth Engine is used to train 400 points from visual inspection and classify the image using texture information from the Sentinel-1 data. The image classification process uses Grey-level co-occurrence measures (GLCM) which provide texture information from each image band (i.e. HH). In this case, we use only the co-polar band instead of the cross-polar and product bands previously described. We calculate the variance, contrast, entropy and ASM (eq. 1-4) for each band to train our classifier in which P is the probability of the matrix in (i, j), for the pixel value and μ representing the mean pixel value of the matrix.

$$\text{Variance} = \sum_{i,j=1}^{N} P_{i,j} \, (i - \mu_i)^2 \text{ and } \sum_{i,j=1}^{N} P_{i,j} \, (i - \mu_j)^2 \quad (1),$$

$$\text{Contrast} = \sum_{i,j=1}^{N} P_{i,j} \, (i - j)^2 \quad (2),$$

$$\text{Entropy} = \sum_{i,j=1}^{N} P_{i,j} \left(-\ln \left(P_{i,j}\right)\right) \quad (3),$$

$$\text{ASM} = \sum_{i,j=1}^{N} P_{i,j}^2 \quad (4),$$

The statistical measures are overlain with the training point image and classified using a support vector machine method as described in Williams et al. (2022).

Results and Discussion

Figure 5: Backscatter intensity (db) changes from March 1 and March 30 2018 in the Amundsen Sea.

The red-outlined flooded regions in the ice field are sampled to retrieve their backscatter intensity. Figure 5 shows the change in the backscatter intensity from the beginning and end of March. March 1 shows a backscatter intensity of ~6.97 ± 1.75 dB and March 30 shows ~9.43 ± 1.94 dB.

The March 1 plot shows backscatter intensities that suggest a more uniform scene. That is, there is more first-year/thin ice than on March 30. There is a leftward shift in the histogram distribution from March 1 to March 30. This is because of the background brightening of the scene as the ice consolidates with freezing temperatures. As the onset of freezing begins at the end of March, the ice surrounding the flooded floes increases in backscatter intensity (tend towards 0 dB) while the slushy, darkened flooded ice floes maintain lower backscatter intensities (dB higher in negative magnitude).

The brining of the slush layer affects the dielectric constant of the icefield. That is, the change in the backscatter intensity of the freezing ice surrounding the flooded floes can affect the adjacent signature of the slush layer. That is, there is a contrast in the backscatter intensities between dry-frozen and brine-flooded ice floes. Therefore, texture information from entropy and contrast grey-level co-occurrence can further separate flooded and unflooded floes. In tandem with incident angle and other SAR factors, the flooded floes display varied backscatter intensities across the ice field. The appropriate image correction techniques and segmentation can be applied to the SAR scenes to separate flooded ice from other water-laden ice features (e.g. ice on open water).

The results of the classification technique describe flooded ice floes as similar in backscatter intensity as thin ice in the context of the co-polar SAR band. Figure 6 shows the results of the classification during the time of the cruise within the spacio-temporal frame of satellite datasets. Figure 7 shows the distribution of IceSat-2 tracks within the February – March timeframe in 2021.

Figure 6: Mean backscatter intensity (db) changes between February and March 2021 within the Weddell Sea. Along the x-axis is the backscatter intensity (db) and along the y-axis is the PDF.

While the flooded ice backscatter intensity shows good agreement between days, the use of the single, co-polar band could still be contributing to variance in the mean values. However, since the increase in standard deviation appears as the scenes transition into March, the change in backscatter intensity may be attributed to a change in the atmospheric conditions as winter approaches and the ice begins to consolidate and solidify. Still, the machine learning technique is more efficient in sequestering the flooded ice from other features in the sea cover. We attempt validation of this finding by investigating changes in the ice thickness in Figure 7 using IceSat-2 and PS-124 ice core data.

Figure 7: IceSat-2 tracks with Polarstern-124 track and core data sampling in Weddell Sea.

The ice core and IceSat-2 data show similar values in ice thickness between February and March 2021. There are spatio-temporal discrepancies between the IceSat-2, buoy and Sentinel-1 imagers. However, MODIS suggests that track lines from IceSat-2 overlap with flooded, thick ice cover in the study area. While this is promising in terms of an approximate net-zero change in thickness, this study would require more in-situ data collection to verify the absolute ice thickness in the scene. This is because the cycle of ice creation and circulation makes satellite imagery limited in the ability to quantify changes in the same ice floe.

Author Contributions

JW was the primary producer of the study, processed and analyzed all the data. SFA, AMM-N and GM all contributed to the design and discussed the results of the study. JW, SFA and AMM-N contributed to the editing of the manuscript.

Competing interests

The authors declare no competing interest.

Financial support

This work was funded by NASA CAMEE grant#: 80NSSC19M0194.

Acknowledgments

We'd like to thank NASA CAMEE grant#: 80NSSC19M0194 for funding this research. Thanks to the Google Earth Engine and its affiliate platforms for allowing cloud computation of data and analysis. Thank you to Sharon Stammerjohn and Stephen Ackley for access to the Polarstern buoy data. We also thank the European Space Agency (ESA) for hosting and allowing API access to Sentinel-2 data to support our findings as well as Earthdata for hosting IceSAT-2 data. Finally, thanks to the ArcGIS Pro, StackExchange and StackOverflow communities for aiding coding research.

References

1. Ackley SF, Perovich DK, Maksym T, Weissling B, Xie H. Surface flooding of Antarctic Summer Sea ice. Annals of Glaciology. 2020 Jun 11;61(82):117–26. doi:10.1017/aog.2020.22.

2. Ackley SF, Fritsen CH, Lytle VI, Sullivan CW. Freezing driven upwelling in Antarctic sea ice biological systems. In Proceedings of the NIPR Symposium on Polar Biology. 1996. 9:45-59. National Institute of Polar Research.

3. Arndt S, Willmes S, Dierking W, Nicolaus M. Timing and regional patterns of snowmelt on Antarctic sea ice from passive microwave satellite observations. (2016). Journal of Geophysical Research: Oceans, 121(8), 5916-5930.

4. Eicken H, Lange MA, Wadhams P. Characteristics and distribution patterns of snow and meteoric ice in the Weddell Sea and their contribution to the mass balance of sea ice. Annales Geophysicae. (1994). Jan 31;12(1):80–93. doi:10.1007/s00585-994-0080-x.

5. Filipponi F. Sentinel-1 GRD preprocessing workflow. 3rd International Electronic Conference on Remote Sensing. 2019 Jun 4; doi:10.3390/ecrs-3-06201.

6. Fritsen CH, Priscu JC. Photosynthetic characteristics of cyanobacteria in permanent ice covers on lakes in the McMurdo Dry Valleys, Antarctica. 1996. Antarctic Journal of the United States, 31(2), 216-218.

7. Golden KM, Ackley SF, Lytle VI. The percolation phase transition in sea ice. Science. 1998 Dec 18;282(5397):2238–41. doi:10.1126/science.282.5397.2238.

8. Hosseinmostafa AR, Lytle VI, Jezek KC, Gogineni SP, Ackley SF, Moore RK. Comparison of radar backscatter from Antarctic and Arctic Sea Ice. Journal of Electromagnetic Waves and Applications. 1995 Jan 1;9(3):421–38. doi:10.1163/156939395x00569.

9. Jeffries MO, Krouse HR, Hurst-Cushing B, Maksym T. Snow-ice accretion and snow-cover depletion on Antarctic first-year sea-ice floes. Annals of Glaciology. (2001). 33:51–60. doi:10.3189/172756401781818266.

10. Jeffries MO, Shaw RA, Morris K, Veazey AL, Krouse HR. Crystal structure, stable isotopes (δ18O) and development of sea ice in the Ross, Amundsen, and Bellingshausen seas, Antarctica. (1994). Journal of Geophysical Research 99(C1):985–995.

11. Lohse J, Doulgeris AP, Dierking W. Incident angle dependence of Sentinel-1 texture features for sea ice classification. (2021). Remote Sensing, 13(4), 552.

12. Lytle VI, Ackley SF. Snow-ice growth: A fresh-water flux inhibiting deep convection in the Weddell Sea, Antarctica. Annals of Glaciology. (2001). 33:45–50. doi:10.3189/172756401781818752.

13. Macdonald GJ, Ackley SF, Mestas-Nuñez AM, Blanco-Cabanillas A. Evolution of the dynamics, area, and ice production of the Amundsen Sea Polynya, Antarctica, 2016–2021. (2023). The Cryosphere, 17(2), 457-476.

14. Maksym T, Jeffries MO. Phase and compositional evolution of the flooded layer during snow-ice formation on Antarctic sea ice. (2001). Annals of Glaciology, 33, 37-44.

15. Massom RA, Eicken H, Hass C, Jeffries MO, Drinkwater MR, Sturm M, Worby AP, Wu X, Lytle V, Ushio S, Morris K, Reid PA, Warren SG, Allison I. Snow on Antarctic sea ice. (2001). Reviews of Geophysics, 39(3), 413-445.

16. Murashkin D, Spreen G, Haas C, Istomina L, Kauker F, Ludwig V. Observation of the 2018 North Greenland polynya with a new merged optical and passive microwave sea ice concentration dataset. (2019). The Cryosphere Discussions, 1-36. doi: 10.5194/tc-2019-23.

17. Necsoiu M, Lewis MJ, Parra J, Hwang P, Wilkinson J, Maksym T, Floricioiu D, Weissling B, Xie H, Ackley S. Studies of Antarctic sea ice characteristics using surface sea ice measurements and TerraSAR-X data. In Presented at the Proceedings of the 4th TerraSAR-X Science Team Meeting, Oberpfaffenhofen. (2001).

18. Ozsoy-Cicek B, Kern S, Ackley SF, Xie H, Tekeli AE. Intercomparisons of Antarctic sea ice types from visual ship, radarsat-1 sar, Envisat Asar, QuikSCAT, and AMSR-e satellite observations in the Bellingshausen Sea. Deep Sea Research Part II: Topical Studies in Oceanography. 2011 May;58(9–10):1092–111. doi:10.1016/j.dsr2.2010.10.031.

19. Perovich DK, Elder BC, Claffey KJ, Stammerjohn S, Smith R, Ackley SF, Krouse HR, Gow AJ. Winter sea-ice properties in Marguerite Bay, Antarctica. (2004). Deep Sea Research Part II: Topical Studies in Oceanography, 51(17-19), 2023-2039.

20. Scharien RK, Segal R, Nasonova S, Nandan V, Howell SE, Haas C. Winter Sentinel-1 backscatter as a predictor of spring Arctic sea ice melt pond fraction. (2017). Geophysical Research Letters, 44(24), 12-262.

21. Tian L, Gao Y, Weissling B, Ackley SF. Snow-ice contribution to the structure of sea ice in the Amundsen Sea, Antarctica. Annals of Glaciology. 2020 Jul 23;61(83):369–78. doi:10.1017/aog.2020.55.

22. Weeks WF, Ackley SF. The growth, structure, and properties of Sea Ice. The Geophysics of Sea Ice. 1986;9–164. doi:10.1007/978-1-4899-5352-0_2.

23. Williams J, Ackley S, Mestas-Nunez A. Lead detection with sentinel-1 in the Beaufort Gyre using Google Earth engine. 2022 Jan 9; doi:10.1002/essoar.10509955.1.

24. Willmes S, Haas C, Nicolaus M. High radar-backscatter regions on Antarctic Sea-ice and their relation to sea-ice and snow properties and meteorological conditions. (2011). International Journal of Remote Sensing, 32(14), 3967–3984. doi:10.1080/01431161003801344.

25. Worby AP, Massom RA, Allison I, Lytle VI, Heil P. East Antarctic Sea Ice: A review of its structure, properties and Drift. Antarctic Sea Ice: Physical Processes, Interactions and Variability. 1998. Mar 22;41–67. doi:10.1029/ar074p0041.

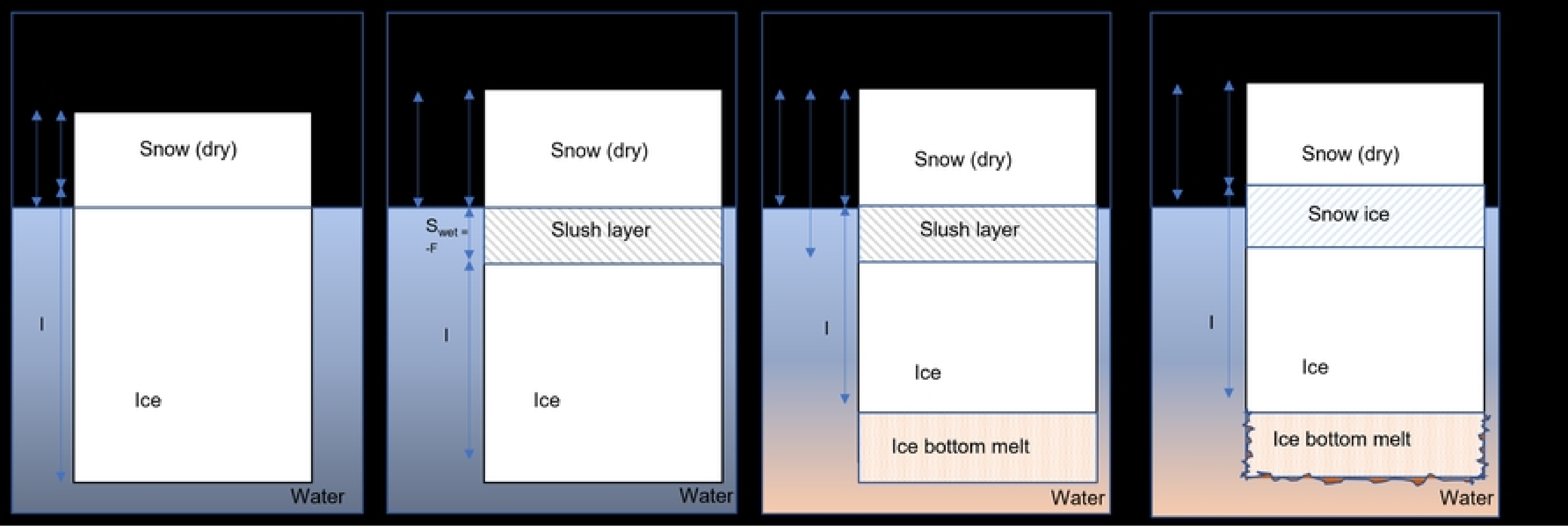
Snow (dry)
Ice
Water
Snow (dry)
Slush layer
S_{wet} =
-F
I
Ice
Water
Snow (dry)
Slush layer
I
Ice
Ice bottom melt
Water
Snow (dry)
Snow ice
I
Ice
Ice bottom melt
Water

Fig1

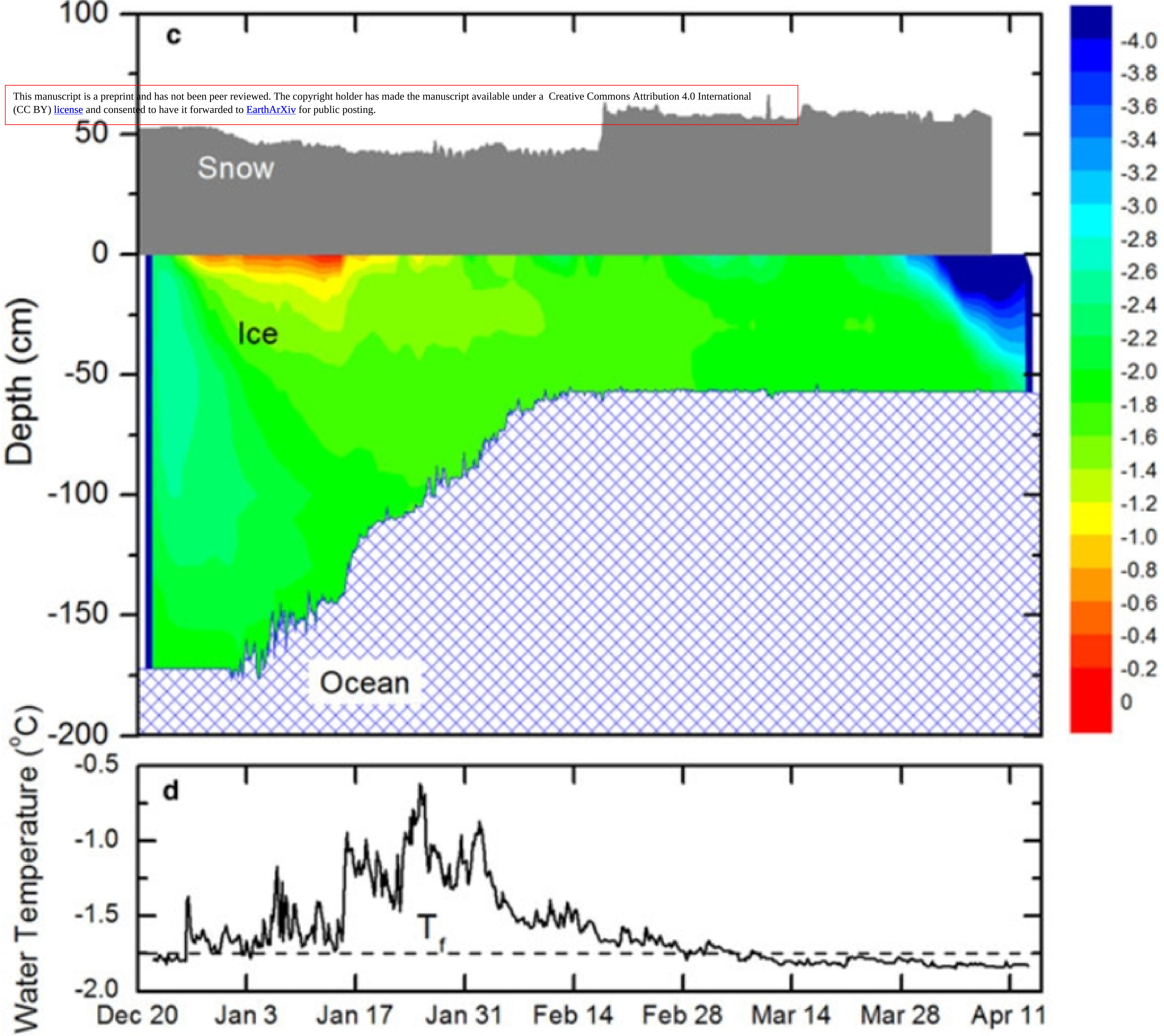
c
Snow
Ice
Ocean
Depth (cm)
100
50
0
-50
-100
-150
-200
-4.0
-3.8
-3.6
-3.4
-3.2
-3.0
-2.8
-2.6
-2.4
-2.2
-2.0
-1.8
-1.6
-1.4
-1.2
-1.0
-0.8
-0.6
-0.4
-0.2
0
d
Water Temperature (°C)
-0.5
-1.0
-1.5
-2.0
T
f
Dec 20
Jan 3
Jan 17
Jan 31
Feb 14
Feb 28
Mar 14
Mar 28
Apr 11

Fig2

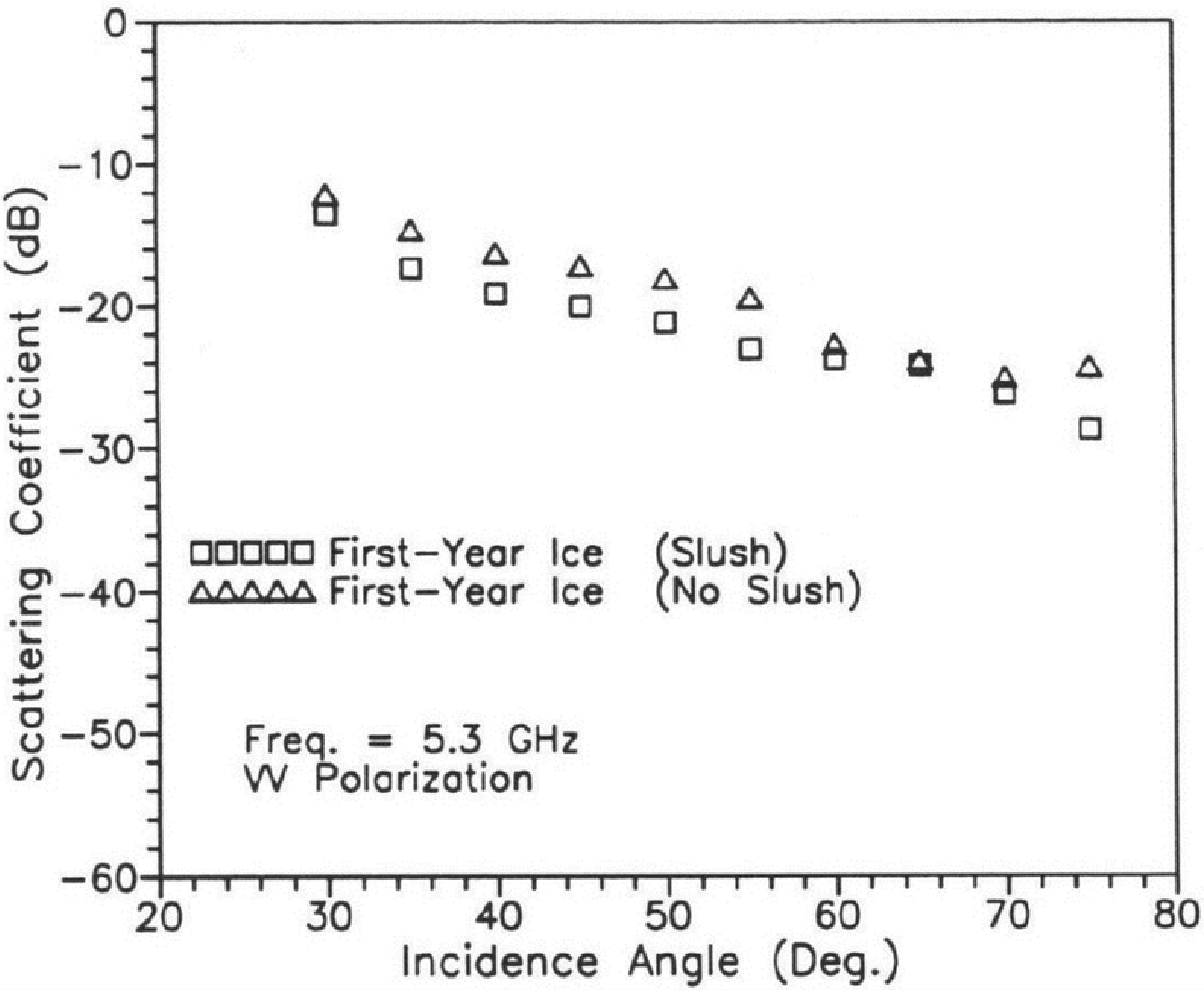
0
−10
−20
−30
−40
−50
−60
20
30
40
50
60
70
80
Scattering Coefficient (dB)
Incidence Angle (Deg.)
First−Year Ice (Slush)
First−Year Ice (No Slush)
Freq. = 5.3 GHz
VV Polarization

Fig3

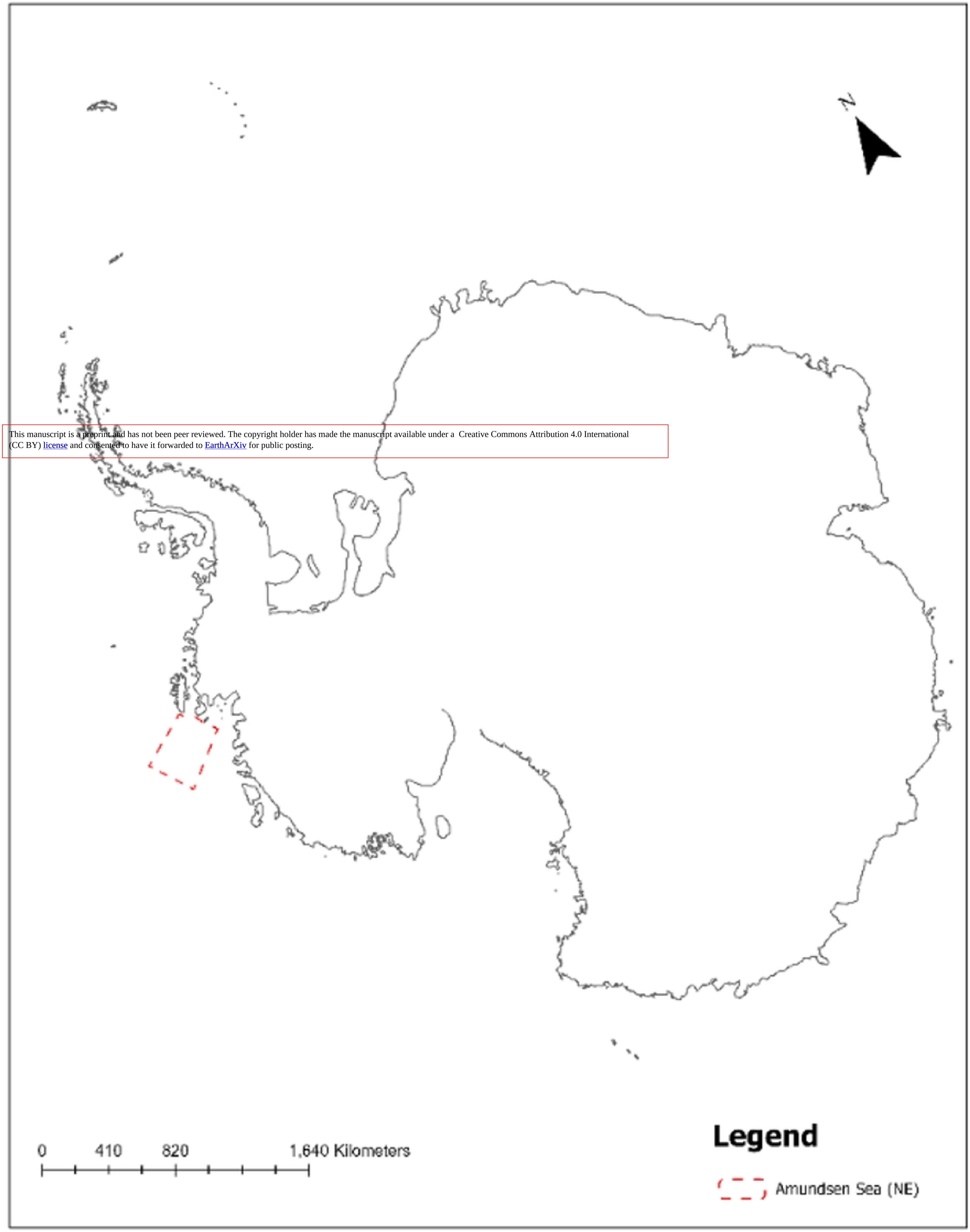

Fig4a

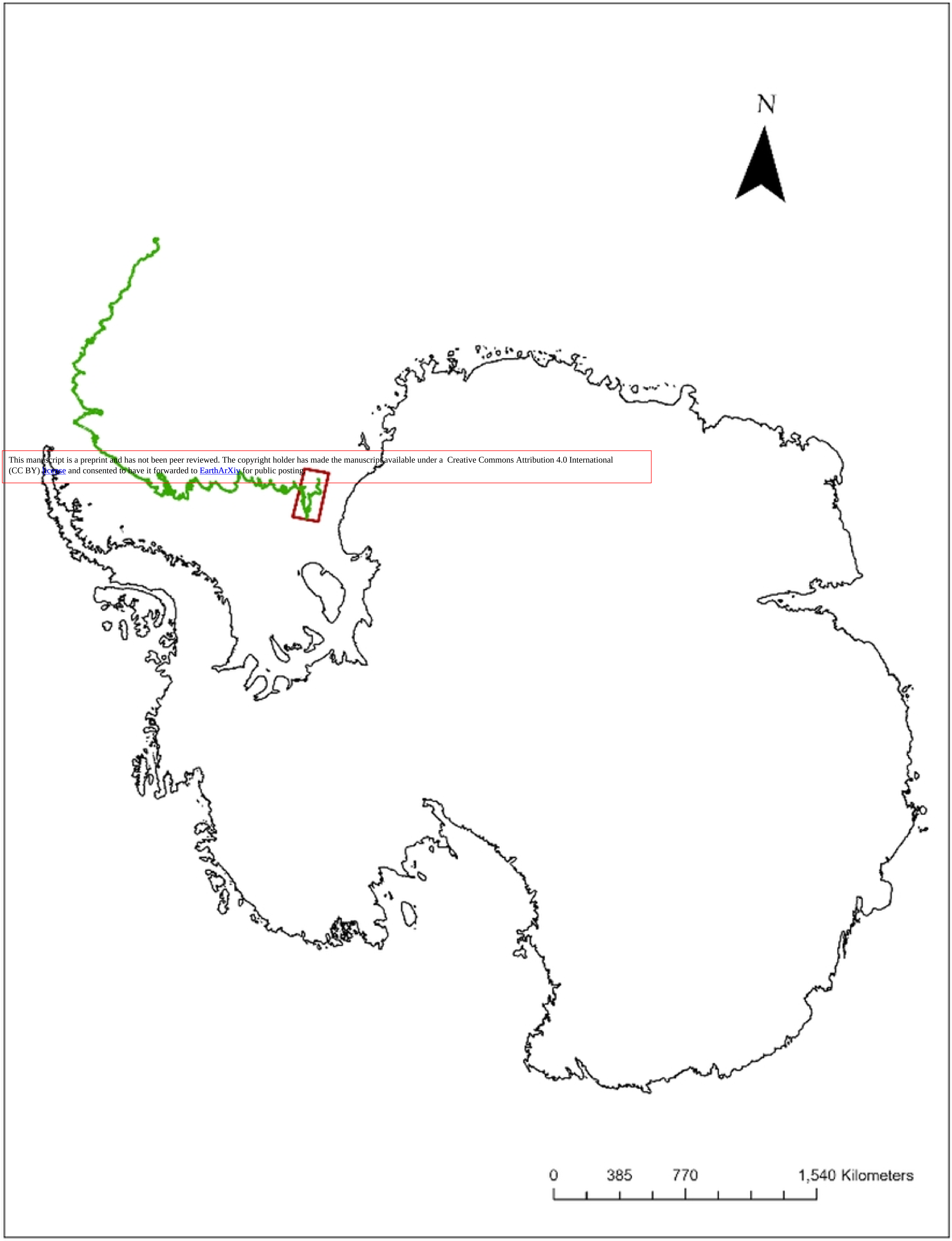

Fig4b

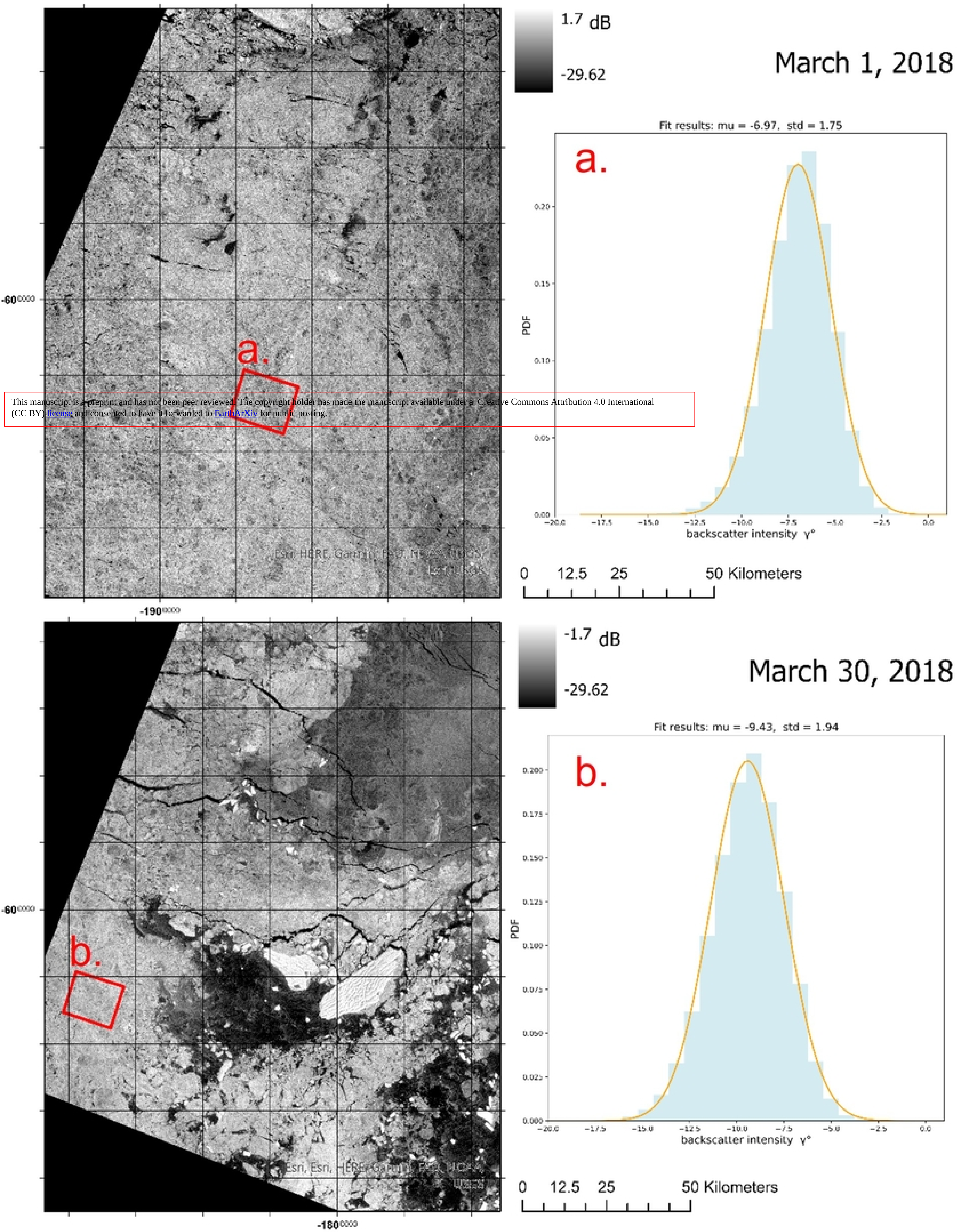
1.7 dB
-29.62
March 1, 2018
Fit results: mu = -6.97, std = 1.75
a.
PDF
backscatter intensity γ°
-60
-190
Esri, HERE, Garmin, FAO, NOAA, USGS,
EPA, NPS
0 12.5 25 50 Kilometers
-1.7 dB
-29.62
March 30, 2018
Fit results: mu = -9.43, std = 1.94
b.
PDF
backscatter intensity γ°
-60
-180
Esri, Esri, HERE, Garmin, FAO, NOAA,
USGS
0 12.5 25 50 Kilometers

Fig5

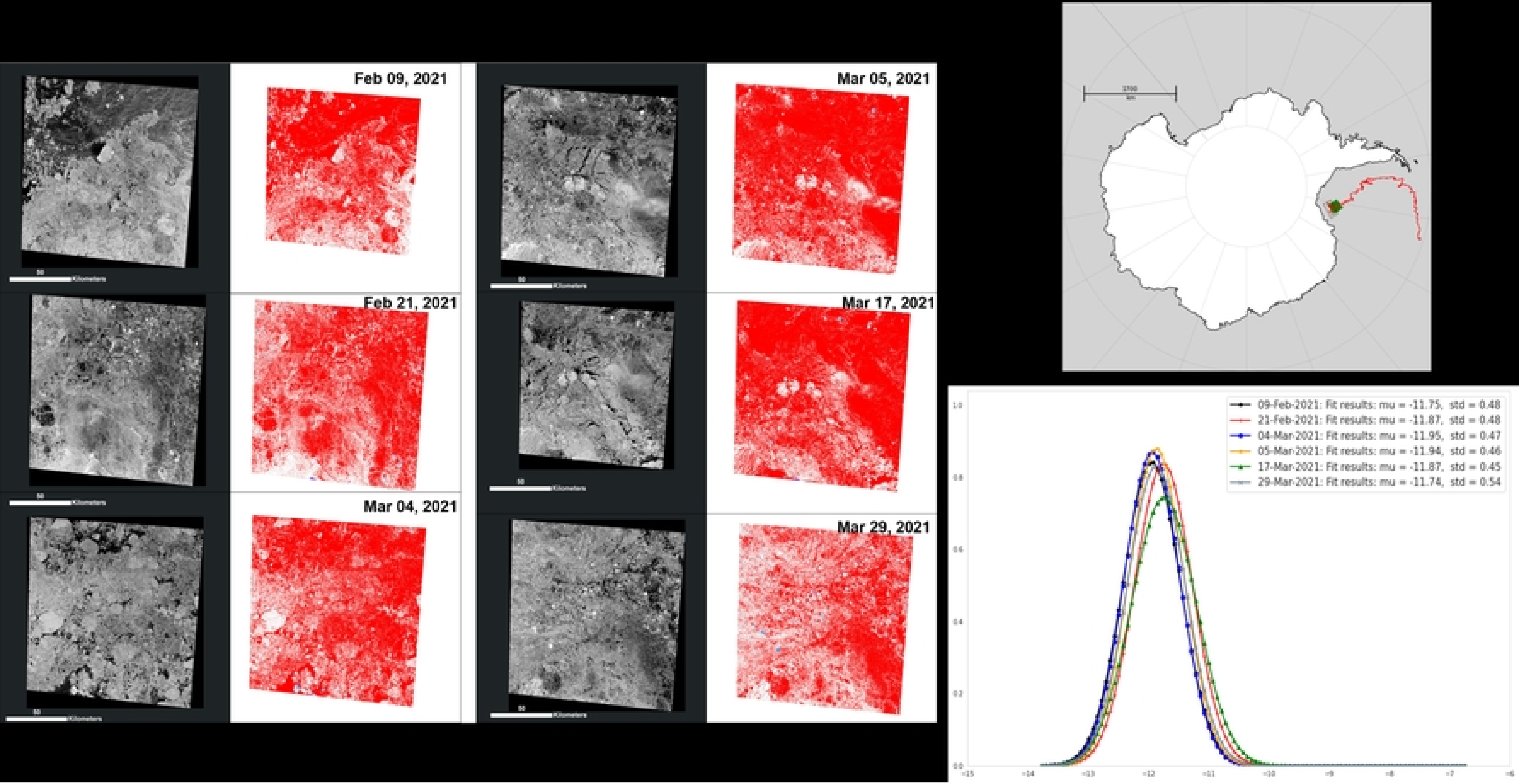

Feb 09, 2021
Feb 21, 2021
Mar 04, 2021
Mar 05, 2021
Mar 17, 2021
Mar 29, 2021
09-Feb-2021: Fit results: mu = -11.75, std = 0.48
21-Feb-2021: Fit results: mu = -11.87, std = 0.48
04-Mar-2021: Fit results: mu = -11.95, std = 0.47
05-Mar-2021: Fit results: mu = -11.94, std = 0.46
17-Mar-2021: Fit results: mu = -11.87, std = 0.45
29-Mar-2021: Fit results: mu = -11.74, std = 0.54

Fig6

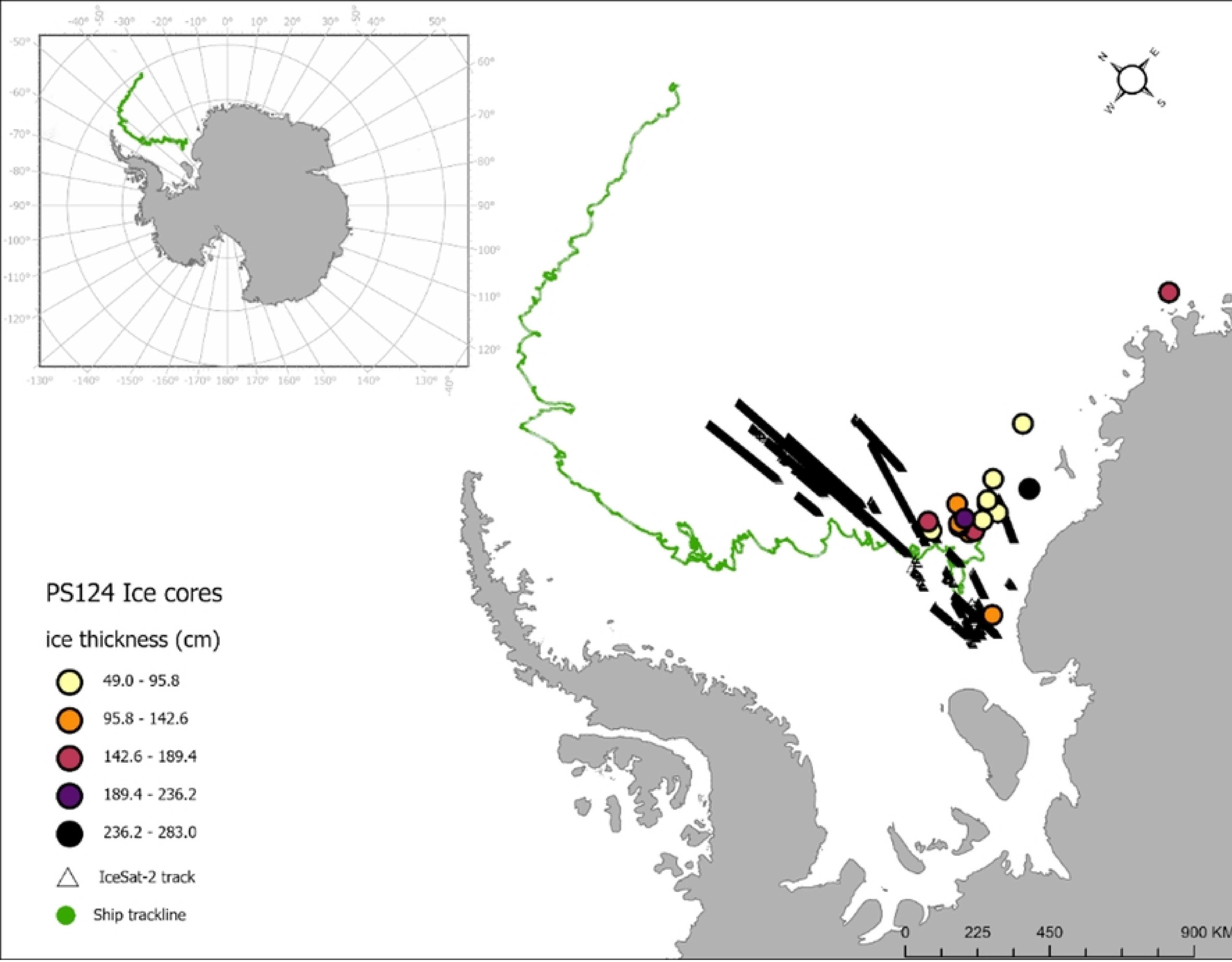
PS124 Ice cores
ice thickness (cm)
49.0 - 95.8
95.8 - 142.6
142.6 - 189.4
189.4 - 236.2
236.2 - 283.0
IceSat-2 track
Ship trackline
0
225
450
900 KM
N
E
S
W

Fig7